



Effect of Shocked Impact of 50 Scaling on the Structural, Morphological, Optical, and Electrical Properties of MMTC Crystals for Correlated Sensor, Photonic, and Piezoelectric Functionalities

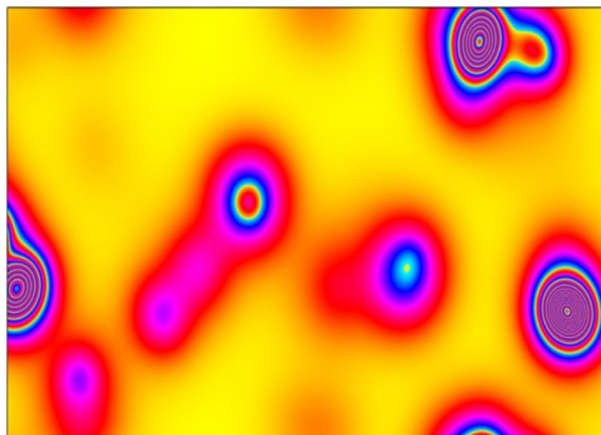
K. Suganya¹ · K. SenthilKannan² · R. Hariharasuthan³ · V. Swarnalatha⁴ · M. Meena⁵ · T. Rajesh Kumar⁶ · R. Manikandan¹

Received: 17 April 2024 / Accepted: 14 June 2024 / Published online: 4 July 2024
© The Minerals, Metals & Materials Society 2024

Abstract

Manganese mercury thiocyanate (MMTC), a nonlinear optical organometallic single-crystal material, was successfully grown by the Sankaranarayanan-Ramasamy (SR) method. The as-grown MMTC crystals were subjected to 50 shock pulses and designated as MMTC50S. The lattice parameters were measured by single-crystal x-ray diffraction (XRD) with values of a , b , and c of 11.3150 Å, 11.3150 Å, and 4.2720 Å with a tetragonal system for the pure MMTC, and values of 11.3180 Å, 11.3180 Å, and 4.2737 Å for MMTC50S, respectively. Fourier transform infrared (FTIR) spectroscopy was used to identify the functional groups present in the MMTC50S crystal. Scanning electron microscopy (SEM) was used to assess the surface morphology, which revealed a pattern of minor defects and minor dislocations in the MMTC50S crystal in contrast to the pure form because of the shock pulses on the MMTC crystal to create the MMTC50S specimen. The UV-visible spectrum showed increased absorption for the MMTC50S crystal. Fluorescence (FL) studies revealed blue fluorescence emission for MMTC50S. Dielectric measurements were carried out and the dielectric constant was calculated for the grown sample. The piezoelectric coefficients and sensor response at room temperature were also determined for MMTC and MMTC50S. The maximum sensitivity for the MMTC50S with a red light-emitting diode (LED) was 8.88%, whereas the blue LED achieved 9% sensitivity.

Graphical Abstract



Keywords Electronic · Photonic · FTIR · Fluorescence · Piezoelectric · Sensor

Extended author information available on the last page of the article

Introduction

A major goal in scientific research is the identification and synthesis of novel crystals for wider application in fields such as communication, where micro-electronics is the predominant parameter for growth.^{1,2} Crystal engineering and crystallography are emerging fields experiencing rapid development in communications, micro-devices, optoelectronics, and fabrication. Among the necessary qualities, flawless crystal is the key parameter in fabrication for the development of nonlinear optical (NLO) crystal with improved second-harmonic generation (SHG) efficiency for better application potential in frequency conversion and phase matching.

The most preferred class of crystalline materials for device fabrication today is organometallic crystals, with their unique properties including charge transfer and transmission, which are important parameters for NLO use.^{3,4} Specifically, hyper-coordinated oxygen, sulfur, or nitrogen atoms are attributable to intramolecular interactions between the organometallic clusters.^{5–9} The highly unique nature of these specimens is the presence of soft donor atomic species, which contributes to their versatile geometry.^{10–12} The improved NLO result is due to the bimetallic types of ligands, mainly thiocyanate (SCN) crystals. This is owing to the easily locomotive electronic device use and charge transfer with larger value of NLO-SHG.^{13–18}

An extraordinary representation in the construction of NLO material is by thiocyanate (SCN) involved in the synthesis of coordinated clusters with metal ions such as cadmium, manganese, zinc, and mercury. Studies of coordinated compounds have identified better NLO-SHG types of materials.^{19–21} One compound demonstrating excellent properties is manganese mercury thiocyanate (MMTC). Structurally, it has Mn^{2+} and Hg^{2+} as two strong electron acceptors and SCN ligand as the major electron donor.

This compound is characterized by an intermediate structure between the small inorganic materials and larger complex macro materials and is a member of the family of two-metal-centered complex crystal compounds.^{22–30} Although various methods have been adopted for the synthesis of MMTC, existing approaches such as SR and other methods are still faced with challenges; thus the synthesis of larger, defect-free specimens is still an important goal of the research community. Therefore, methods are needed for the growth of good-quality macro-sized crystals of MMTC to enhance their application potential.^{29–31}

Experimental Synthesis and Reaction Mechanism of MMTC

MMTC was synthesized using ammonium thiocyanate, mercury chloride, and manganese chloride as reactants. Chemical agents of high purity were used for the chemical reaction, which is specified as follows:



The MMTC crystal was properly synthesized and purified by recrystallization with the use of solubility details to overcome the concentration gradient, and the solution was mixed continuously for 24 h in a magnetic stirrer. The crystals were successfully grown over a period of 7–8 days. The process was effectively enabled by spontaneous nucleation with the room temperature. Good-quality, defect-free MMTC crystals were identified for further experiments and properly harvested. The b-cut MMTC crystal with thickness of 2×10^{-3} m was grown using the customary SR method. A temperature of 50°C was consistently maintained on all sides of the growth zone to maintain the proper stability. The growth of the crystal was enhanced and was clearly seen within 5–6 days as crystal seed formation and was finally harvested within 7–8 days. A thin layer of the solution in the zone between the ampoule and growing crystal. The fully formed crystal was seen after 40 days with proper dimensions. Also, a shock pulse with pressure of 2 MPa with 2.2 Mach shock wave pulses at a temperature of 864 K was considered with three different categories of 50, 100, and 150 shock pulses, and here the MMTC crystal sample with 50 shock pulses, designated as MMTC50S, is used.

XRD

The lattice parameters were measured by single-crystal x-ray diffraction studies with values of *a*, *b*, and *c* of 11.315 Å, 11.315 Å, and 4.272 Å with a tetragonal system with non-centrosymmetric space group $\bar{14}$ for the pure MMTC and values of 11.3180 Å, 11.3180 Å, and 4.2737 Å for MMTC50S, respectively, as shown in Table I for ease

Table I Single-crystal XRD data of MMTC and MMTC50S crystals

Crystal	MMTC ^{16–18}	MMTC50S
<i>a</i>	11.3150 Å	11.3180 Å
<i>b</i>	11.3150 Å	11.3180 Å
<i>c</i>	4.2720 Å	4.2737 Å
System	Tetragonal	
Alpha, beta, and gamma	Each 90°	
Space group	$\bar{14}$	

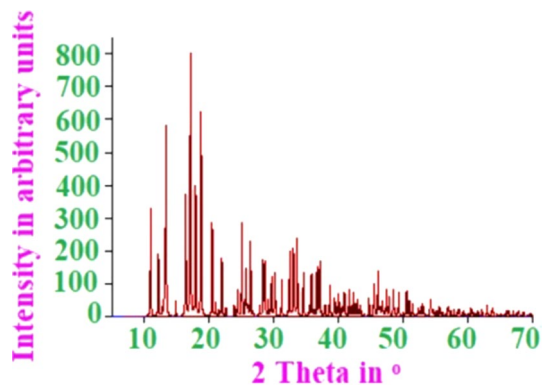


Fig. 1 Powder XRD pattern of MMTC50S crystal.

of comparison. The difference in peaks versus the pristine sample^{16–18} is due to the impact of 50 shock pulses on the specimen. The powder XRD (PXRD) pattern of MMTC50S is shown in Fig. 1 at 2θ angles of 0° – 70° and 0–800 arbitrary units of PXRD intensity, and the pure/irradiated samples are compared for reference with earlier MMTC work.^{16–18}

FTIR Analysis of MMTC50S Crystal

The Fourier transform infrared (FTIR) spectrum of the MMTC shocked impact crystals was recorded in the range of 4000 – 400 cm^{-1} . The freshly ground MMTC50S samples showed a band at 2128 cm^{-1} attributed to CN stretching vibrations within this range, and a band appearing between 895 and 776 cm^{-1} was attributed to CS stretching vibrations (N bonding). A peak at 466 cm^{-1} was ascribed to SCN bending vibrations (N bonding) and a band at 444 cm^{-1} corresponded to SCN bending vibration (S-bonding). These results show that the CN stretching of NH_4SCN is slightly shifted from 2085 cm^{-1} to 2128 cm^{-1} in the present sample, which confirms the presence of the thiocyanate group which is linked with the metal ions through the sulfur and nitrogen. The two weakest absorption bands in the spectra at 895 and 776 cm^{-1} were due to the effect of N bonded, S bonded CS stretching of the compounds, respectively, which is the normal behavior response of ABTC type structural materials. The bending vibration of the SCN was absorbed at 466 cm^{-1} , which was evidence of the coordination of the SCN ligand, and a weak bond was observed near that; thus the N and S type bonded materials were properly identified using FTIR analysis for the MMTC50S crystals as shown in Fig. 2.

Optical Studies of MMTC50S Crystal

The grown shocked impact on MMTC crystal was analyzed for UV-visible and fluorescence studies. The absorbance spectrum of the MMTC50S crystal showed a major

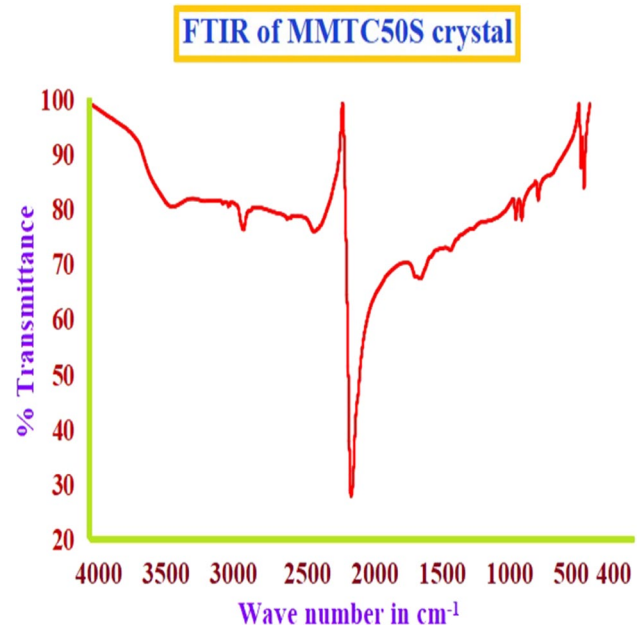


Fig. 2 FTIR spectra of MMTC50S crystal.

shift in the absorption peak towards the lower-wavelength region due to the shocked impact on the MMTC crystal. The results indicate the effect of absorption around 263 nm for the MMTC crystal of shocked impact. The absorbance peaks decreased when the shocked impact was increased due to the lattice defect in a minor level induced on the sample. Over the total range of 200 – 1100 nm , the values from 300 nm to 1100 nm revealed nearly zero absorbance, which implies that the transmittance is greater, which is required in material for nonlinear applications, especially of higher-order NLOs. The cutoff wavelength is 263 nm , which gives a bandgap value of 4.7148 eV . The fluorescence (FL) spectrum of MMTC50S showed emission at 484 nm resulting in a bandgap of 2.5619 eV related to blue fluorescence emission, so blue fluorescence emission was demonstrated by the MMTC50S specimen. Therefore, the energy value was increased because the fluorescence peak value was smaller than that of the pure crystal, as a result of the impact of the shock pulses over the sample. This fluorescence emission may have potential use in biochemical, biomedical, and material-related applications. Figures 3a, b and 4 illustrate the absorbance, Tauc's plot, and the FL data for the MMTC50S crystal. The bandgap by the direct approach using Tauc's plot for $1/n$ substituted $1/2$ leads to power 2 of y-axis components, and the value of the bandgap by photonic energy versus $(\alpha h\nu)^2$ gives the photonic utility of MMTC50S with 4.72 eV by Tauc and 4.7148 by absorbance data using UV-visible data. A variance of 0.0052 variance is observed.

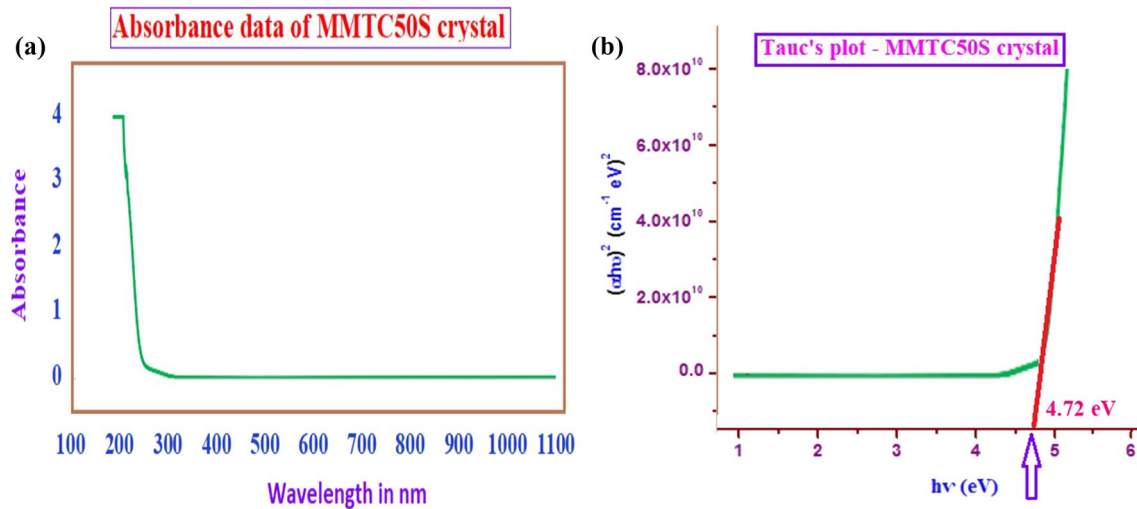


Fig. 3 (a) Absorbance data for MMTC50S crystal. (b) Tauc's plot of MMTC50S crystal.

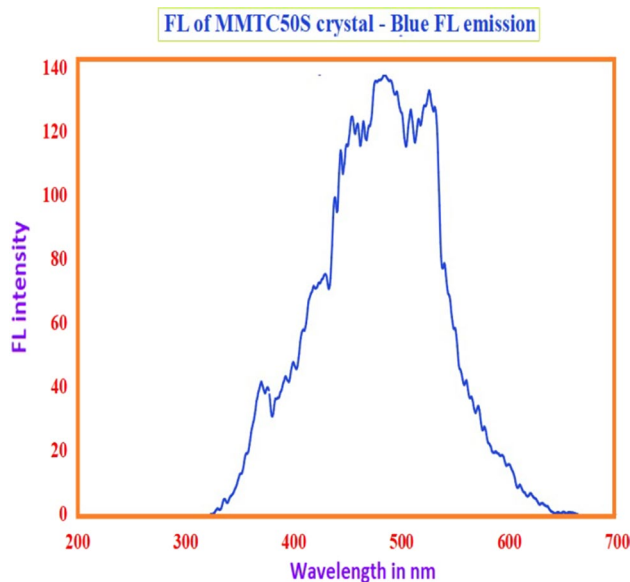


Fig. 4 FL data of MMTC50S crystal for blue FL emission.

SEM investigation of MMTC50S Crystal and Electronic Studies of Different MMTC Samples

The surface morphology of the MMTC50S crystal was investigated by scanning electron microscopy (SEM, ZEISS). Some isolated islands were present in the specimen, and SEM analysis at a voltage of 10,000 V with SE1 signal, and width of 10 mm, magnified around 3000 times, shows only a rock-like structure with no flaws, and no major cracks are observed after the shock pulses, only the small islands and some of the deepest fingerprint observed for the specimen MMTC50S as shown in Fig. 5 for 10 μm scaling.

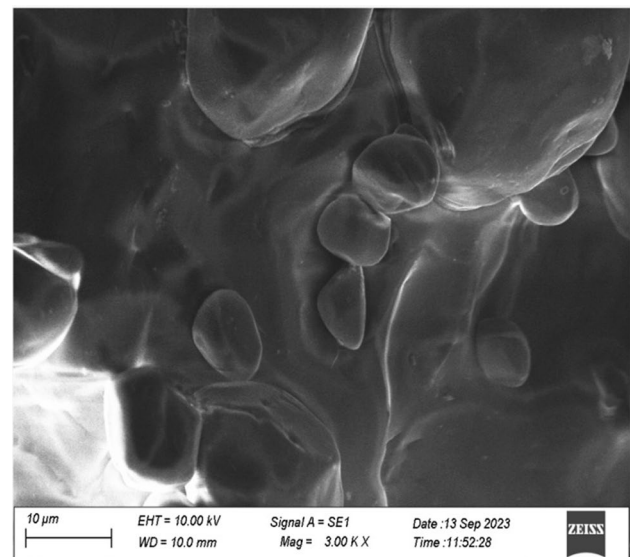


Fig. 5 SEM of MMTC50S crystal.

The materials of the MMTC crystal as per space group are of non-centrosymmetric case of representing SHG-NLO,¹⁶ is subjected to frequency doubling and the output frequency is double the input one for the normal case and is 2.13 and 2.16 times for the MMTC and MMTC50S veneered samples for frequency enhancers. The voltage regulation using diodes is increased by 2.4% for MMTC and 3.2% for the MMTC50S coated components for use as regulated power supply control applications. The electronic filter influx is 2.8956 microns and 2.9972 microns for MMTC and MMTC50S for opto-electronic filter use.

Dielectric Studies of MMTC50S Crystal

The dielectric properties of the MMTC50S were analyzed, including the dielectric constant and dielectric loss. An interrelation exists between the electro-optics and the dielectric values of crystalline materials, and the current study shows the variation in the dielectric constant and dielectric loss at room temperature for varying frequency values along the x -axis. The dielectric constant is higher in the low-frequency region, at a value of nearly 95, and slowly decreases to near zero as the frequency is increased; there is also a zigzag variation in the dielectric constant values. The dielectric loss starts at 1.45 and slowly decreases when the frequency is increased, with two or three places showing zigzag variation. The zigzag variation for the dielectric loss and dielectric constant is due to the impact of the shock pulse on the MMTC crystals, and the decrease in the dielectric constant at low frequencies is due to the association of electronic and ionic orientation and space charge polarization. This represents the purity and perfect nature of the material towards the space charge in the low-frequencies region. The higher dielectric constant in the low-frequency region represents the defects present at the grain boundary. Compared to the pure MMTC crystal, the higher dielectric constant and dielectric loss values for the MMTC50S crystal are due to the impact of the shock pulses. The increasing frequency and corresponding decreasing loss indicate moderately better quality of the MMTC50S crystal versus the pure crystal specimen. The high dielectric loss in the lower-frequency region is due to the space charge polarization. The change in the dielectric loss and dielectric constant compared to the pure crystal is due to the impact of the shock pulse and the bond length and bond angle variation by the shock pulses, which in turn produces a zigzag effect at the middle range

of the $\log f$ values of the dielectric constant and larger $\log f$ values of the frequencies at the dielectric loss parameters. Thus, one can conclude that the dielectric loss and dielectric constant increase with an increase in the number of shock pulses. Here, 50 shock pulses are used, as shown in Fig. 6a and b, and further 100 and 150 pulses will be enabled.

Piezoelectric (PE) Effect and Room-Temperature-Based Sensor Studies of MMTC and MMTC50S Crystalline Samples

The MMTC and MMTC50S crystals are subjected to PE measurement systematically using a piezometer¹⁷ at room temperature. To improve the electrical outcome, the surfaces are coated with high-grade Ag. The PE charge coefficient (denoted as d_{33} pC/N) for MMTC is 3.6 pC/N in the recorded frequency range of 50–300 Hz and for MMTC50S is 3.8 pC/N. The PE charge coefficient, or PE modulus, describes the change in volume when the PE specimen is subjected to an electric field, showing the induced effect of polarization along the z -axis when stress is along the z -axis and d_{31} stress is along the x -axis. After polling, no variance in the PE charge coefficient is observed for each case owing to the existence of a saturation polarization effect in the crystalline specimens. Figure 7a and b present the inverse PE effect and comparison of the coefficients of MMTC and MMTC50S using bar charts. The room-temperature-supported sensor action of MMTC and MMTC50S at 28.6° C with 52.4% and 53% humidity reveals that the max of 5400 s on the x -axis and the 1 for counts–intensity values along the y -axis show the variance in both cases. For MMTC, the linear fit for y of $7 \times 10^{-5} x + 0.2301$ with R^2 of 0.1743 gives 7.77% sensitivity of the MMTC, whereas the MMTC50S, with y of $8 \times 10^{-5} x + 0.1876$ and R^2 of 0.2466, achieves 8.88% sensitivity.

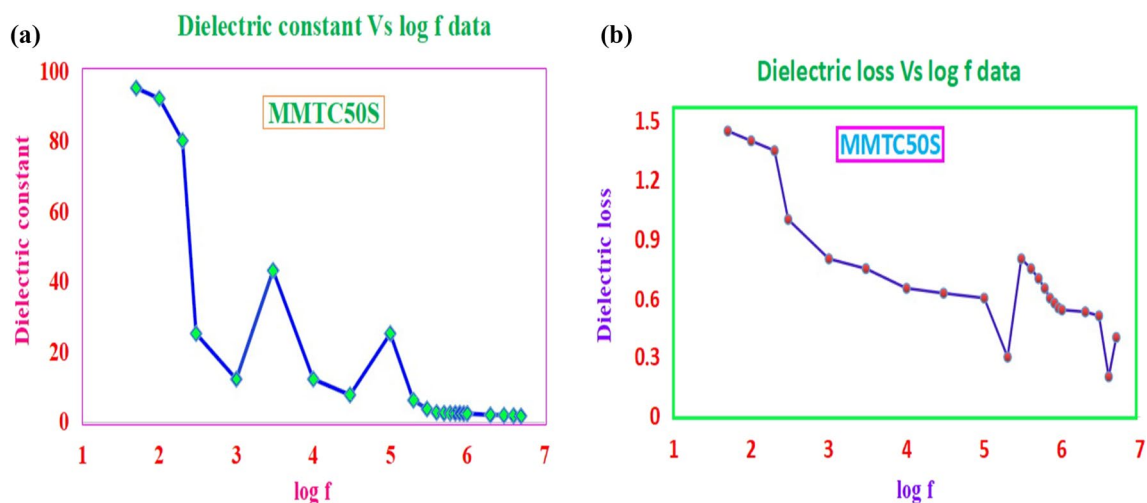


Fig. 6 (a) Dielectric constant of MMTC50S crystal. (b) Dielectric loss of MMTC50S crystal.

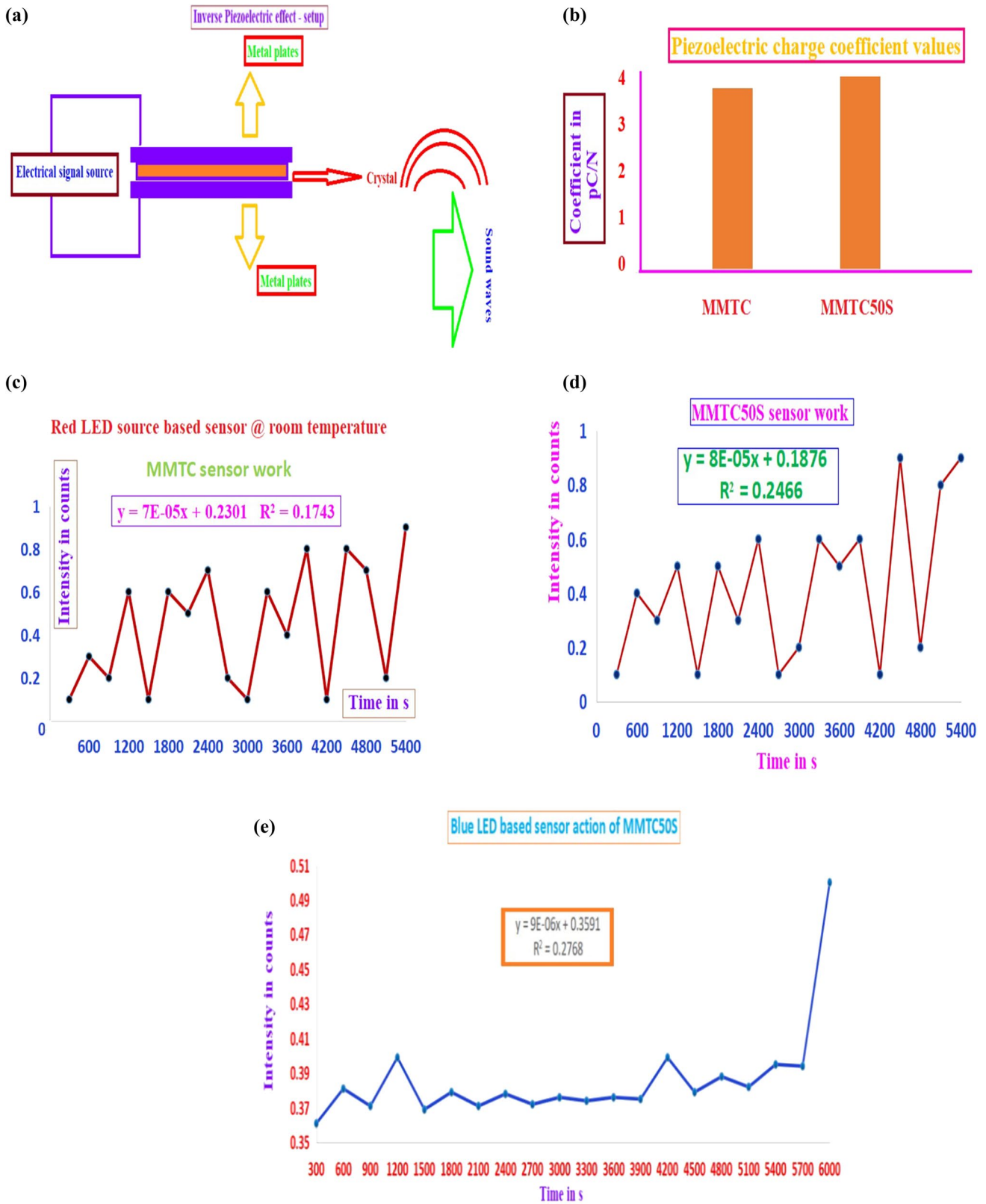


Fig. 7 (a) Inverse piezoelectric setup for strain output. (b) Bar chart comparison of MMTC and MMTC50S for piezoelectric coefficients. (c) Red LED-based room-temperature sensor effect of MMTC crystal. (d) Red LED-based room-temperature sensor effect of MMTC50S crystal. (e) Blue LED-based room-temperature sensor effect of MMTC50S crystal.

Between the MMTC and MMTC50S, for PE and sensor applications, MMTC50S is thus preferred given the values and sensitive nature, as shown in Fig. 7c and d for MMTC and MMTC50S, respectively.^{16–18} The blue light-emitting diode (LED)-based sensor work of MMTC50S, showing time varying from 0 to 6000 s and intensity from 0.31 to 0.51 counts with y of $9 \times 10^{-6}x + 0.3591$ and R^2 of 0.2768, gives blue LED sensitivity of 9%, and the pure with other shocked impact is further reported soon for blue LED work near future.

Display Profile, Void Space, and Cloned Impact of MMTC Crystal

The computational analysis of the MMTC crystal is shown for the projected display and the spacing and gap inside the solid crystal and the cluster combination of mapping of interactions using software tools. The MMTC crystal is analyzed for the (101) Miller index profile with distance of 6.7545 Å from the origin with Z_{\min} and Z_{\max} of 0.002 and 11.25 for Y-M-C (yellow, magenta, cyan) with recursive mapping of saturation of maximum value of 0.9964 (0.38%) and minimum value of -0.0001 (-0.001%) for the (101) mode as shown in Fig. 8a. The void spacing of MMTC is

shown in Fig. 8b with the median voids of the crystal, and the clustered cloned impact of MMTC for the normalized profile of interaction is shown in Fig. 8c for harboring/thermal mapping for further analysis.

Results and Discussion

In this work, MMTC is effectively synthesized using ammonium thiocyanate, mercury chloride, and manganese chloride as reactant materials to synthesize the MMTC50S crystal. The crystals are successfully grown over a period of 7–8 days.

The lattice parameters are measured by single-crystal x-ray diffraction studies with values of a , b , c of 11.315 Å, 11.315 Å, and 4.272 Å with a tetragonal system with non-centrosymmetric space group $\bar{14}$ for the pure MMTC and values of 11.3180 Å, 11.3180 Å, and 4.2737 Å for MMTC50S, respectively.

The FTIR spectrum of the MMTC shocked impact crystals is recorded in the range of 4000–400 cm^{-1} . Freshly crushed MMTC50S samples are measured for FTIR data and the functional groups are reported.

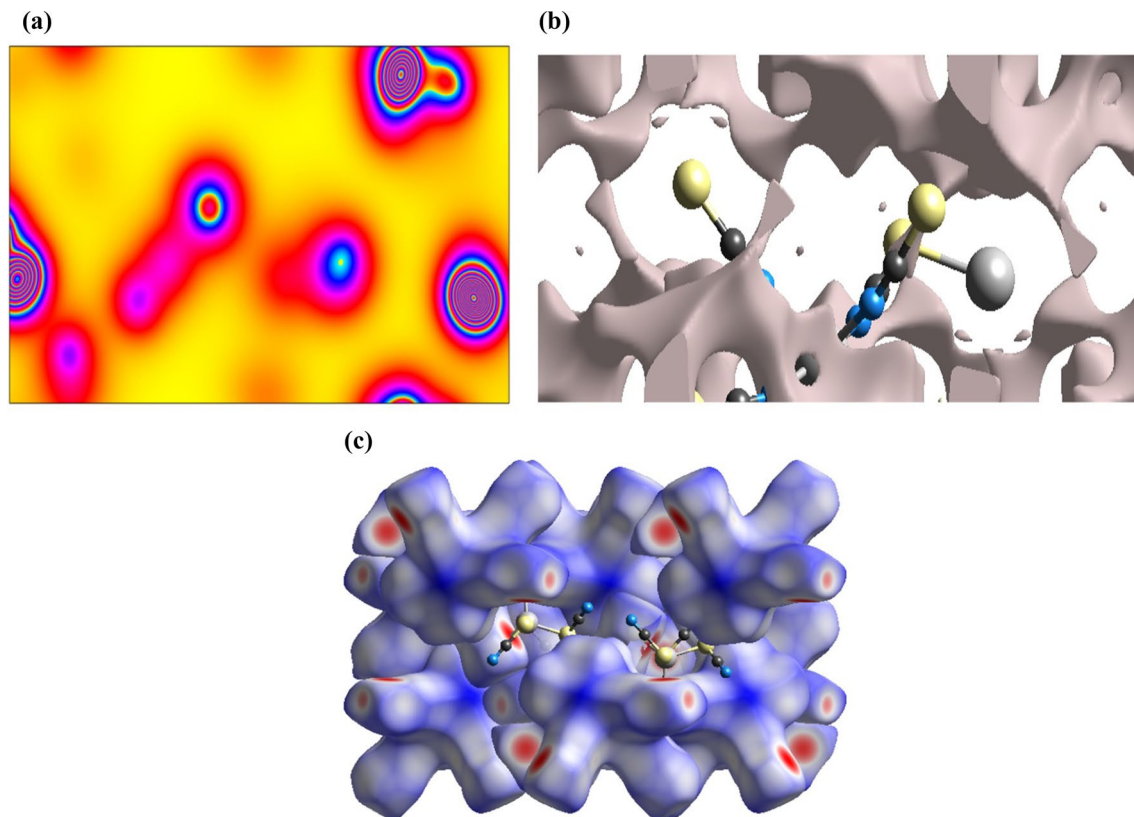


Fig. 8 (a) YMC (101) profile of MMTC crystal. (b) Void spacing of MMTC crystal. (c) Cloned clustering of normalized interaction mapping of MMTC crystal.

The results show the effect of absorbance with a cutoff wavelength of 263 nm which gives a bandgap value of 4.7148 eV. The fluorescence (FL) spectrum of MMTC50S shows fluorescence emission at 484 nm, which gives a bandgap of 2.5619 eV related to the fluorescence emission, which is blue in color, thus indicating blue fluorescence emission from the MMTC50S specimen.

Analysis of the surface morphology of the MMTC50S crystal (ZEISS SEM) shows some isolated islands present in the specimen, with no flaws, and no major cracks are observed after the shock pulse, only the small islands and some of the deepest fingerprint observed for the specimen MMTC50S as mentioned for 10 μm scaling.

The increase in the dielectric constant at low frequencies is due to the association of electronic and ionic orientation and space charge polarization. This represents the purity and perfect nature of the material towards the space charge in the lower-frequency region. The higher dielectric constant in the low-frequency region represents the defects present at the grain boundary. Compared to the pure MMTC crystal, the higher dielectric constant and dielectric loss values for the MMTC50S crystal are due to the impact of the shock pulses. The increasing frequency and corresponding decreasing loss indicate the moderately better quality of the MMTC50S crystal versus the pure crystal specimen. The charged lattice defects represent the larger dielectric loss in the lower-frequency region which is due to the impact of the space charge polarization. The change in the dielectric loss and dielectric constant compared to the pure crystal is due to the impact of the shock pulse and the bond length and bond angle variation by the shock pulses.

The PE charge coefficient (d_{33} pC/N) of MMTC is 3.6 pC/N in the recorded frequency range of 50–300 Hz and 3.8 pC/N for MMTC50S. The room-temperature-supported sensor action of MMTC and MMTC50S of 28.6°C with humidity of 52.4% and 53% concerned with max of 5400 s as the x -axis and 1 as counts–intensity values along the y -axis show variance in both cases. For MMTC, the linear fit of y as $7 \times 10^{-5} x + 0.2301$ with R^2 of 0.1743 gives 7.77% MMTC sensitivity, whereas the MMTC50S with y of $8 \times 10^{-5} x + 0.1876$ with R^2 of 0.2466 gives 8.88% MMTC50S sensitivity. Between MMTC and MMTC50S, for piezoelectric and sensor applications, MMTC50S is preferred by the values and sensitivity for MMTC and MMTC50S, respectively. The blue LED work shows 9% sensitivity for MMTC50S.

The MMTC crystal was analyzed for the (101) Miller index profile with a distance of 6.7545 Å from the origin, with Z_{min} and Z_{max} of 0.002 and 11.25 for Y-M-C [yellow, magenta, and cyan] with recursive mapping for the (101) mode; also, the void spacing of MMTC is characterized by median voids of the crystal, and the clustered cloned impact of MMTC for

normalized interaction profile for harboring/thermal mapping for further analysis.

Conclusion

A nonlinear optical MMTC single crystal was grown using the SR method. The MMTC single crystal was properly developed through exposure to 50 shock pulses and designated as MMTC50S. The parameters of the pure MMTC crystal compound were $a = 11.315 \text{ \AA}$, $b = 11.315 \text{ \AA}$, and $c = 4.272 \text{ \AA}$ with a tetragonal system. The shocked MMTC50S parameters were $a = 11.3180 \text{ \AA}$, $b = 11.3180 \text{ \AA}$, and $c = 4.2737 \text{ \AA}$. The functional group of the MMTC50S crystal was clearly identified from the FTIR spectra. The SEM analysis showed that the surface morphology of the MMTC50S crystal was characterized by minor defects and minor dislocations in contrast to the pure form of MMTC. The absorbance value of MMTC50S was increased by UV-visible spectra. The fluorescence study of MMTC50S showed emission spectra with blue fluorescence related to the shocked form of the compound. Dielectric measurements were carried out and the dielectric constant/loss were calculated for the grown sample. The computational data indicated potential for use in devices and for piezoelectric and sensor-based applications for the MMTC and MMTC50S crystals. The blue LED work showed 9% sensitivity for MMTC50S, greater than for red LEDs.

Acknowledgments The authors would like to thank Mr Vincent Sagararaj of St. Joseph's College for the studies and IITM for data and Phoenix Institute for electronic studies; also, would like to thank Prof. Dr. S.A.M. Britto Dhas, Sacred Heart, for providing samples.

Author Contributions K Suganya: Assisting in crystal growth, cleaning the specimen and electronic work. K Senthil Kannan: XRD, SEM, sensor, piezoelectric work, write-up & submission. R Hariharasuthan: UV, FL work. V Swarnalatha: FTIR work, shocked write-up. M Meena: Computational work. T. Rajesh Kumar: Crystal growth by SR method. R Manikandan: Dielectric work and overall correction of paper.

Funding This work received no funding, and the authors provided their own funding for this paper.

Data Availability All the data associated with this paper are included in the article; there is no separate repository or representation of data.

Conflict of interest On behalf of all authors, the corresponding author states that there is no conflict of interest.

Ethical approval The manuscript has not been submitted anywhere else previously or simultaneously, and is an original work.

References


1. M. Selvapandiyan, S. Sudhakar, and P. Sundaramoorthi, Crystal growth, structural, spectral and mechanical studies of pure and KI doped ZTS single crystals. *J. Alloys Compd.* 523, 25 (2012).

2. Y. Wu and W. Bensch, Synthesis, crystal structures, and optical properties of NaCdPnS₃ (Pn =As, Sb). *J. Alloys Compd.* 511, 35 (2012).
3. P.W. Zukowski, S.B. Kantorow, D. Maczka, and V.F. Stelmakh, Processes of radiation defect interaction and amorphisation of silicon at large implantation doses. *Phys. Status Solidi A* 112(2), 695 (1989). <https://doi.org/10.1002/pssa.2211120225>.
4. X.Q. Wang, D. Xu, M.K. Lu, D.R. Yuan, S.X. Xu, S.Y. Guo, G.H. Zhang, and J.R. Liu, Crystal growth and characterization of a novel organometallic nonlinear-optical crystal: MnHg(SCN)₄(C₂H₆O)₂. *J. Cryst. Growth* (2001). [https://doi.org/10.1016/S0022-0248\(01\)01012-0](https://doi.org/10.1016/S0022-0248(01)01012-0).
5. D.G. Vargas-Pineda, T. Guardado, F. Cervantes-Lee, A.J. Meta-Magaña, and K.H. Pannell, Intermolecular Chalcogen-Tin Interactions in [(*o*- MeEC₆H₄)CH₂]₂SnPh_{2-n}Cl_n (E = S, O, CH₂; n = 0, 1, 2) and intermolecular Chlorine – Tin Interactions in the *meta*- and *para*- Methoxy Isomers. *Inorg. Chem.* 49(3), 960 (2010). <https://doi.org/10.1021/ic901800c>.
6. R.A. Varga, K. Jurkschat, and C. Silvestru, Solid-state structure and behavior in solution of hypervalent organotin(IV) derivatives containing 2-(Me₂NCH₂)C₆H₄ moieties. *Eur. J. Inorg. Chem.* (2008). <https://doi.org/10.1002/ejic.200701044>.
7. Z. Rappoport, *The chemistry of organic germanium, tin and lead compounds*, Vol. 2 (UK: Wiley, 2002).
8. R. Cea-Olivares, V. García-Montalvo, and M.M. Moya-Cabrera, The importance of the transannular secondary bonding strength in the molecular structures of metalocenes of type [X(CH₂CH₂Y)₂MRR'] and [X(CH₂CH₂Y)₂M'R] (M= Ge(IV), Sn(IV), Pb(IV), M' = As(III), Sb(III) and Bi(III); X=NR", O, S; Y=O, S). *Coord. Chem. Rev.* 249(7–8), 859 (2005). <https://doi.org/10.1016/j.ccr.2004.10.002>.
9. M.P. Coles, M.S. Khalaf, and P.B. Hitchcock, A new aliphatic N, C, N'-pincer ligand with pendant guanidine groups. *Inorg. Chim. Acta* 422, 228 (2014).
10. A.G. Davies, M. Gielen, K.H. Pannell, and E.R.T. Tiekink, *Tin chemistry: fundamentals frontiers and applications* (UK: Wiley, 2008).
11. C. Pellerito, L. Nagy, L. Pellerito, and A. Szorcik, Biological activity studies on organotin(IV)^{pn+} complexes and parent compounds. *J. Organomet. Chem.* (2006). <https://doi.org/10.1016/j.jorganchem.2005.12.025>.
12. J.E. Le Grogneq, J.M. Chrétien, F. Zammattio, and J.P. Quintard, Methodologies limiting or avoiding contamination by organotin residues in organic synthesis. *Chem. Rev.* 115, 10207 (2015).
13. X.Q. Wang, X.F. Cheng, S.J. Zhang, D. Xu, G.H. Zhang, Z.H. Sun, F.P. Yu, X.J. Liu, W.L. Liu, and C.L. Chen, Single crystal growth, structural characterization, thermal and optical properties of a novel organometallic nonlinear optical crystal: MnHg(SCN)₄(C₂H₅NO)₂. *Phys. B* 405, 1071 (2010).
14. X.Q. Wang, D. Xu, M.K. Lu, D.R. Yuan, J. Huang, G.W. Lu, G.H. Zhang, S.Y. Guo, H.X. Ning, X.L. Duan, Y. Chen, and Y.Q. Zhou, A systematic spectroscopic study of four bimetallic thiocyanates of chemical formula AB(SCN)₄: ZnCd(SCN)₄ and AHg(SCN)₄ (A= Zn, Cd, Mn) as UV nonlinear optical crystal materials. *Opt. Mater.* 23, 335 (2003).
15. X.Q. Wang, D. Xu, M.K. Lu, D.R. Yuan, G.H. Zhang, F.Q. Meng, S.Y. Guo, M. Zhou, J.R. Liu, and X.R. Li, Investigation of bimetallic thiocyanates belonging to ABTC structure type: ZnCd(SCN)₄ and AHg(SCN)₄ (A=Zn, Cd, Mn) as nonlinear optical crystal materials. *Cryst. Res. Technol.* 36, 73 (2001).
16. X. Vasanth Winston and D. Sankar, Gamma ray-irradiated induced effects on SCN ligand-based MMTC single crystals for optoelectronic applications synthesized by SR method. *J. Mater. Sci. Mater. Electron.* (2022). <https://doi.org/10.1007/s10854-022-08873-8>.
17. S. Barlow and S.R. Marder, Nonlinear optical properties of organic materials. *Funct. Org. Mater.: Synth, Strateg. Appl.* (2006). <https://doi.org/10.1002/9783527610266.ch11>.
18. R. Josephine Usha, P. Sagayaraj, and V. Joseph, Linear and nonlinear optical, mechanical, electrical and surface of a novel nonlinear optical crystal: manganese mercury thiocyanate (MMTC). *Spectrochim. Acta Part A Mol. Biomol. Spectrosc.* (2014). <https://doi.org/10.1016/j.saa.2014.04.161>.
19. G.H. Gilmer, R. Ghez, and N. Cabrera, An analysis of combined surface and volume diffusion process in crystal growth. *J. Cryst. Growth* 8, 79 (1971).
20. T. Rajesh Kumar, R. Jersld Vijay, R. Jeyasekaran, S. Selvakumar, M. Antony Arockiaraj, and P. Sagayaraj, Growth, linear and nonlinear optical and laser damage threshold studies of organometallic crystal of MnHg(SCN)₄. *Opt. Mater.* 33, 1654 (2011).
21. X. Wang, Xu. Dong, Lu. Mengkai, D. Yuan, X. Chang, S. Li, Ji. Huang, S. Wang, and H. Liu, Crystal growth, spectral and thermal properties of nonlinear optical crystal: MnHg(SCN)₄. *J. Crystal Growth.* 245, 126 (2002).
22. X. Liu, X. Wang, Z. Sun, X. Lin, Xu. Guanghui Zhang, and Dong, Study on micro-crystallization, growth, optical properties and defects of a nonlinear optical crystal: MnHg(SCN)₄. *J. Cryst. Growth* 317, 92 (2011).
23. R.K. Raju, S.M. Dharmaparakash, and H.S. Jayanna, Gamma irradiation effects on crystalline and optical properties of pure and doped Potassium hydrogen phthalate (KHP) single crystals. *Optik* 127, 11649 (2016).
24. R. Hariharasuthan, K.S. Radha, Z. Abdul Vaheith et al., Electronic, nano-dielectric, mass and fluorescence spectral characterizations of 2-amino 4-methyl pyridinium fumarate novel crystals for use in opto-electronics and electronic displays. *J. Mater. Sci. Mater. Electron.* (2023). <https://doi.org/10.1007/s10854-023-10158-7>.
25. V. Sathiyaraj et al., Synthesis and studies of the zinc acetate (ZA) crystal for dielectric, nano-photonics and electronic applications. *J. Mater. Sci. Mater. Electron.* (2022). <https://doi.org/10.1007/s10854-022-08787-5>.
26. K. SenthilKannan et al., Characterization of zinc acetate micro-crystals (ZA_μ) and Co-60 irradiated micro-crystals (GZA_μ) for photonic and electro-optic relevance. *J. Mater. Sci. Mater. Electron.* (2023). <https://doi.org/10.1007/s10854-023-10550-3>.
27. A. Sivakumar, S.S.J. Dhas, S. Balachandraraj et al., Impact of shock waves on molecular and structural response of potassium dihydrogen phosphate crystal. *J. Electron. Mater.* (2019). <https://doi.org/10.1007/s11664-019-07605-9>.
28. J.H. Joshi, S.A.M.B. Dhas, D.K. Kanchan et al., Tailoring the low dielectric constant in glutamic acid doped ammonium dihydrogen phosphate single crystal by virtue of MPa shock waves for microelectronic applications: the complex impedance and modulus formulation studies. *J. Mater. Sci. Mater. Electron.* (2020). <https://doi.org/10.1007/s10854-020-04048-5>.
29. R. Sakunthaladevi and L. Jothi, Chemical growth dynamics of 4-methyl-4'-hydroxy benzylidene aniline NLO single crystal structure and spectroscopic applications. *J. Molecular structure.* 1233, 130054 (2021).
30. S. Boomadevi and R. Dhanasekaran, Synthesis, crystal growth and characterization of L-pyrrolidone-2-carboxylic acid (L-PCA) crystals. *J. Crystal Growth* 261, 70 (2004).
31. S. Hinano, P.C. Kim, H. Orihara, H. Umeda, and Y. Ishibashi, Dielectric properties of hydrothermally grown gallium orthophosphate single crystals. *J. Mater. Sci.* 25, 2800 (1990).

Springer Nature or its licensor (e.g. a society or other partner) holds exclusive rights to this article under a publishing agreement with the author(s) or other rightsholder(s); author self-archiving of the accepted

manuscript version of this article is solely governed by the terms of such publishing agreement and applicable law.

Authors and Affiliations

K. Suganya¹ · K. SenthilKannan²  · R. Hariharasuthan³ · V. Swarnalatha⁴ · M. Meena⁵ · T. Rajesh Kumar⁶ · R. Manikandan¹

✉ K. SenthilKannan
msggoldmedalist@yahoo.in

¹ Department of Chemistry, A.V.V.M Sri Pushpam College (affiliated to Bharathidasan University, Tiruchirappalli - 620024), Poondi, Thanjavur, Tamilnadu 613503, India

² Department of Physics, Saveetha School of Engineering, SIMATS, Saveetha University, Chennai, Tamilnadu 602105, India

³ Department of Chemistry, S.A. Engineering College, Poonamalle, Chennai, Tamilnadu 600077, India

⁴ Department of Chemistry, St. Joseph's College of Engineering, OMR, Chennai, Tamilnadu 600119, India

⁵ Department of Chemistry, R.M.K Engineering College, Kavaraipettai, Tamilnadu 601206, India

⁶ Department of Physics, G.T.N. Arts College (Autonomous), Dindigul 624 005, India